Fuel 429 (2027) 140764

Contents lists available at ScienceDirect

Fuel

journal homepage: www.elsevier.com/locate/fuel

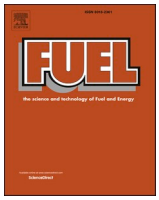

Full Length Article

Spatially resolved *operando* investigations of the CO_2 methanation reaction using DRIFTS and gas phase analysis

Timo Engl [a], David Kellermann [b], Jan Kopyscinski [c], Hannsjörg Freund [b], Michael Rubin [a,*], Roland Dittmeyer [a]

[a] Institute for Micro Process Engineering (IMVT), Karlsruhe Institute of Technology (KIT), Hermann-von-Helmholtz-Platz 1, 76344 Eggenstein-Leopoldshafen, Germany
[b] Institute of Reaction Engineering and Catalysis (REC), TU Dortmund University, Emil-Figge-Straße 66, 44227 Dortmund, Germany
[c] Catalytic & Plasma Process Engineering, McGill University, 3610 University Street, Montreal, Quebec H3A 0C5, Canada

ARTICLE INFO

Keywords:
CO_2 methanation reaction
Load flexibility
Operando DRIFTS
Plate reactor
Reactor modeling
CFD study

ABSTRACT

Power-to-X (PtX) processes using renewable electricity for hydrogen production plus non-fossil CO_2 will be an important part of the future energy system relying also on e.g. synthetic methane. The fluctuating nature of renewable energies, however, represents a challenge since it can propagate all the way through the PtX process chain. For stationary operation with well-defined feed and process conditions, the CO_2 methanation reaction is well understood. However, for tuning catalyst properties and process parameters for transient operation, deeper insights based on fundamental *operando* studies is of crucial importance. In this contribution, we present a unique reactor setup enabling spatially resolved *operando* investigations of both, gas phase composition and species adsorbed on a catalyst surface using gas chromatography and infrared spectroscopy (DRIFTS). The performance of an industrial Ni/Al_2O_3 methanation catalyst was investigated as a function of reaction temperature (100–450 °C) and space velocity (1–20 $ml_N\ mg^{-1}\ min^{-1}$). The spatially resolved DRIFTS (SRD) reactor was modeled, and the flow profile and concentration gradients were simulated using CFD, indicating that the gas sampling does well represent the actual concentration along the reactor coordinate, which was additionally validated by benchmarking to a catalytic plate reactor reference system. The results presented and discussed not only verify the ability of the SRD reactor setup for in-depth investigation but are also in line with the methanation mechanism discussed in literature. Further, the results suggest that the formation of carbonyls which readily react to methane can be seen as the rate-determining step for this type of catalyst.

1. Introduction

The defossilization of the energy system is a path that most countries in the world have embarked on and was agreed on in the Paris Climate Agreement [1]. The transition of electricity generation from fossil sources, such as coal and gas, to renewable energy sources, like wind and solar, plays a crucial role. Making the chemical and energy sector carbon–neutral requires large amounts of renewable electricity and new technologies for generating green feedstock as well as for energy storage and distribution. Here, the so-called Power-to-X technologies, with "X" being molecules with high chemical energy such as methane (renewable natural gas), play a major role [2,3]. In a country with a large industry like Germany, this will require 250–650 TWh of hydrogen and its derivatives alone [4]. In this context, hydrogen is to be produced through water electrolysis using renewable electricity, and the CO_2 needs to be obtained from non-fossil sources, ideally directly from the air (direct air capture), to ensure net-zero CO_2 emissions. Even though the catalytic processes are well researched and understood, to date, they have usually been operated under steady-state conditions and mostly not using green feedstock such as green hydrogen. Since green hydrogen production requires renewable electricity with its inherent variable availability, Power-to-X processes should be capable to be operated under dynamic load to avoid the need for large, costly buffer facilities for electricity and/or hydrogen storage.

For the CO_2 methanation reaction being the focus of this study, a simplified reaction network adapted from Schmider et al. [5] is shown in Fig. 1. According to this scheme, there are mainly two routes for the CO_2 activation and its further reaction to CH_4. On the one hand, there is the CO_2* dissociation to CO* + O* (I) and on the other hand, the hydrogen-assisted CO_2* dissociation via the formate route (II, III and further IV). In

* Corresponding author.
E-mail address: michael.rubin@kit.edu (M. Rubin).

https://doi.org/10.1016/j.fuel.2026.140764
Received 11 May 2026; Received in revised form 22 June 2026; Accepted 20 July 2026
Available online 28 July 2026

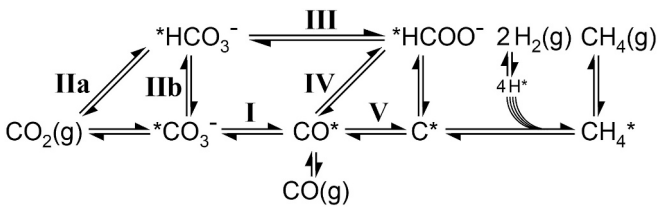

Fig. 1. Simplified reaction network of the methanation reaction adpated from [5]. I) CO_2 dissociation II) H assisted CO_2 dissociation III) formate formation via bicarbonate IV) formate dissociation V) CO* hydrogenation.

both cases (I, IV), the formation of CO* is critical as it serves as a highly active surface intermediate towards CH_4.

In the context of transient operation, such as variations in space velocity, a deeper understanding of the catalyst behavior is essential [6]. Laboratory research reactors with spatially resolved analysis capabilities offer the possibility of gathering a variety of information about a catalyst system along the reactor coordinate, whereas conventional research reactors, often referred to as "end-of-pipe," only provide information about the exit fluid composition. In recent years, there have been a number of publications presenting spatially resolved reactors with movable capillaries as well as non-intrusive methods (UV–VIS, infrared (IR)) to measure gas composition, gas temperature, and catalyst surface temperature along the reactor axis [7–17]. In addition to that, Urakawa et al. [18–21] presented a reactor setup where spatially resolved diffuse reflectance infrared Fourier transform spectroscopy (DRIFTS) can be used to identify the adsorbed species along the reactor axis at three and four locations, allowing for qualitative investigations. The identification of these surface species is essential for the investigation of the reaction mechanism, as they can represent the intermediates of the reaction and gain value through local resolution.

In a prior publication, we presented a tap reactor [22] that allows to analyze gas samples (gas chromatography, GC) taken at five (incl. outlet) points along the reactor and thereby track changes in the gas phase composition as a function of time and location. Compared to reactors allowing for spatially resolved gas analysis via gas sampling using a capillary moving along the reactor coordinate, the tap reactor can gather the concentration profile over 5 different locations along the reactor coordinate within only one minute (11 s per location), thus, enabling fast gas sampling that is not prone to falsifications, e.g. due to catalyst deactivation during the course of gas sampling.

This reactor was further upgraded by adding an optical access for infrared spectroscopy. Compared to the reactors described in the literature, this spatially resolved DRIFTS (SRD) reactor can operate in real time, providing high spatial and temporal resolution of adsorbed species along the reactor length. Data obtained by combining these two methods (GC + DRIFTS) allow for a more detailed understanding of the reaction mechanism of the investigated catalyst and a semi-quantification of the adsorbed species with spatial resolution. This paper presents an *operando* spatially resolved DRIFTS study of the CO_2 methanation with an industrial nickel catalyst (8.2 wt% Ni, 130 $m^2\ g^{-1}$ specific surface area (BET) [23], denoted as industrial methanation reference catalyst, SPP2080-IMRC in the following). This catalyst has been extensively characterized (N_2 physisorption, Hg porosimetry, X-ray tomography (pellet), transmission electron microscopy, X-ray diffraction, long term stability, …) [23,24] by other consortia of the priority project SPP2080 funded by the German Research Foundation, DFG. For a detailed overview of Ni-based catalysts for the CO_2 methanation, also concerning the effects of supports other than Al_2O_3, the interested reader is kindly referred to accordant review articles such as by Xu et al. [25] and Strucks et al. [26] on general aspects and Liu et al. [27] on Ni/CeO_2 catalysts in particular. The reactor used was benchmarked against an established catalytic plate reactor with spatially resolved measurement capabilities [11,15,28,29]. An approach is presented for deriving not only qualitative, but also normalized quantitative information on adsorbed and gas phase species along the reactor length from spatially resolved DRIFT spectra. The spatially resolved data align well with results obtained from variations in space velocity (SV, volumetric flow rate of the reactants per catalyst mass). The method outlined allows for rapid DRIFTS analysis without changing the reaction parameters.

2. Experimental

2.1. Spatially resolved DRIFTS (SRD) reactor and analytics

2.1.1. SRD reactor

The spatially resolved DRIFTS reactor is an adaptation of the tap reactor shown in [22]. Fig. 2 shows the reaction channel into which the reactants enter from the left and exit at the right end. The reaction chamber is a channel (1 mm height, 22 mm width, 143 mm length) equipped with 5 successive catalyst-coated foils (2.2 cm × 2.4 cm each) in recesses at its bottom, representing five individual reaction zones. Between each of the five reaction zones, through-holes with a diameter of 0.8 mm, each connected to a capillary connected to an online GC (Agilent 8860), allow for gas phase sampling and, thus, for obtaining spatially resolved concentration profiles along the reactor (inlet and outlet is likewise connected to GC). The setup enables temporally resolved gas sampling at a fixed spatial position every 22 min, or for spatially resolved gas sampling, which takes 1 min to collect the gas samples for subsequent analysis in the GC. Seven heating cartridges beneath the reactor ensure uniform heating, thermally connected to the reactor body through an 8 mm thick copper plate. The reaction chamber is closed with a CaF_2 crystal window which is transparent for mid-wave infrared light with a transmission of >90 % and allows infrared spectroscopy to be performed on the surface of the catalyst layer (see section 2.1.2 for details). Based on measured temperature profiles (via IR camera through the window of the SRD reactor, see Supporting Information, Fig. S7) under both, inert conditions as well as under reaction conditions (operando) at different set-point (SP) temperatures (300 °C and 400 °C) it can be shown that the temperature differences

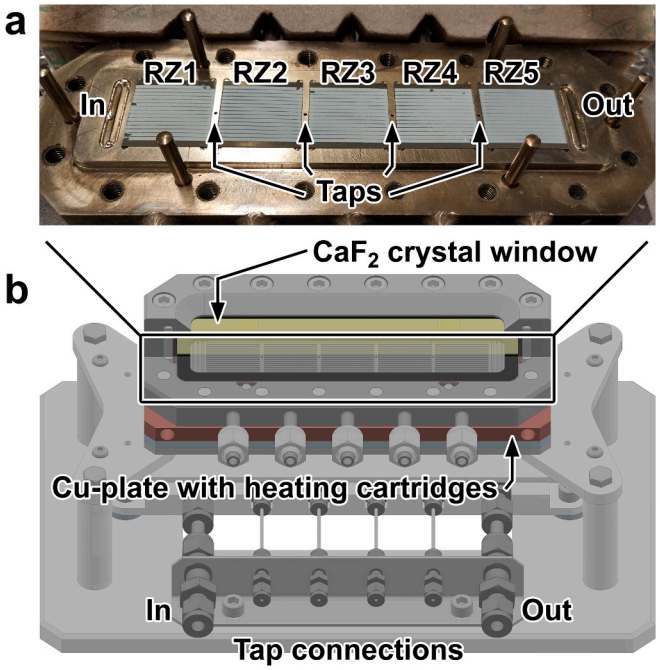

Fig. 2. (a) Top view photograph of the spatially resolved DRIFTS reactor with inlet, outlet, the five reaction zones (RZ) including the catalyst coated onto the microstructured foils and the taps for gas sampling in between. (b) 3D drawing from the whole DRIFTS-reactor assembly incl. CaF_2 crystal window and Cu-plate with heating cartridges.

along the reactor coordinate is in the range of $\Delta T = 5$ K (SP: 300 °C) and $\Delta T = 10$ K (SP: 400 °C), while there is basically no difference between inert atmosphere and reaction conditions. The latter shows that in the SRD reactor the exothermicity of the reaction does not cause a severe temperature increase due to the low catalyst mass resp. thin catalyst layer related to the large thermal inertia of the reactor body (see also Ref. [22]). Calibrated mass flow controllers (Brooks) are used for the gas supply of CO_2, H_2 and N_2. The standard reaction pressure of 5 bar(a) is maintained via a back-pressure regulator at the outlet and was chosen as a compromise between high pressure favoring the methanation reaction [30] and the limitations by implementation of the window for the optical access. The system can be operated automatically to adjust pressure, temperature, gas flow rates and gas phase sampling (GC). The coating of the microstructured foils with the catalyst using screen printing is described in detail in [22].

2.1.2. DRIFTS analysis

For DRIFT spectroscopy, the SRD reactor is equipped with the aforementioned CaF_2 window (thickness: 12 mm); a specially adapted setup was developed. Spatial resolution was achieved by moving the reactor underneath a tailored DRIFTS setup. The top view of the overall setup consisting of the reactor itself, the IR source, light guidance and detector is shown in Fig. 3.

The spectrometer (1, IR cube FT-IR OEM spectrometer from Bruker Optics) has a resolution of 4 cm^{-1} and is used in the wavenumber range of 4000–1000 cm^{-1}. This range covers the absorption bands of the species typically found in CO_2 methanation, such as carbonate, formate, CO_2, CH_4, etc. The infrared beam (2) is directed through a KBr window over a convex gold mirror (4) through the CaF_2 window of the reactor (3) into the reaction chamber, focused on the actual catalyst layer implemented as coating as described above. CaF_2 is particularly transparent in the wavenumber range of 4000–1000 cm^{-1} and therefore ensures clear signals for further evaluation. On its way to the catalyst surface, the infrared light is partially absorbed by the gaseous reactants in the gas phase within the reaction chamber before it interacts with the catalyst surface and the accordant adsorbed species. The catalyst layer is approximately 40 μm thick (measured with profilometry) with a mass distribution of approx. 4 mg cm^{-2}, so the light is diffusely scattered on the surface and in the layer and repeatedly reflected by the catalyst and the species adsorbed on it. A second gold mirror (4) collects a portion of the diffuse reflected light and focuses (5) it into the liquid nitrogen cooled MCT (Mercury Cadmium Telluride) detector (6) where the infrared light eventually is analyzed. Spatially resolved DRIFT spectra are gathered by moving the reactor axially with a linear step motor. Since infrared light is strongly absorbed by CO_2 and H_2O of the ambient air, the ray path including the mirror optics is encased in Plexiglas® and purged with nitrogen to reduce the distorting influence of such components within the ray path. The coupling of DRIFTS analysis with the SRD reactor thus provides spatially resolved *operando* analysis of surface species in combination with spatially resolved gas phase studies. With the number of variable parameters, it is possible to collect a large amount of data in a short time to enable modeling of methanation and potentially also other heterogeneously catalyzed reactions. In a recent publication, we analyzed the temperature resolved spectra of two catalysts using the SRD reactor, which resulted in discovering two different reaction pathways for the respective catalysts [31]. Additionally Kellermann et al. [32] used the reactor setup to investigate time resolved formate and Ni-CO species with a combination of modeling and *operando* investigations.

2.1.3. Experimental procedure

An industrial Ni/Al_2O_3 catalyst (referred to as SPP2080-IMRC, where IMRC stands for industrial methanation reference catalyst) with a particle size of <3 μm was used in the methanation experiments. The catalyst consists of 8.6 wt% nickel supported on aluminum oxide and has been extensively studied in the literature [22–24]. The coating of the micro-structured foils with the SPP2080-IMRC has been described in detail in [22]. The present study focuses on its experimental characterization using the SRD reactor. Five catalyst plates were prepared ($m_{catalyst} = 18.7, 17.5, 22.2, 18.3, 20.1$ mg, $m_{total} = 96.8$ mg) and placed in the reactor. The catalyst was *in-situ* reduced in 50 vol% H_2 in N_2 for 8 h at 400 °C and atmospheric pressure at a flow rate of 300 $ml_N\ min^{-1}$ which are the recommended reduction conditions of the industrial manufacturer of the SPP2080-IMRC. H_2-TPR from Weber et al. [24] for the very same catalyst have shown a reduction temperature above 300 °C to ensure full reduction of NiO to Ni^0. After reduction, the reactor was purged with pure N_2 (99.999 vol%) and pressurized to 5 bar(a).

Background spectra were recorded for DRIFT spectroscopy at the accordant reaction temperature at which the sample spectrum was taken (Volume flow of N_2 equivalent to a SV of 4.6 $ml_N\ mg^{-1}\ min^{-1}$, 5 bar(a))

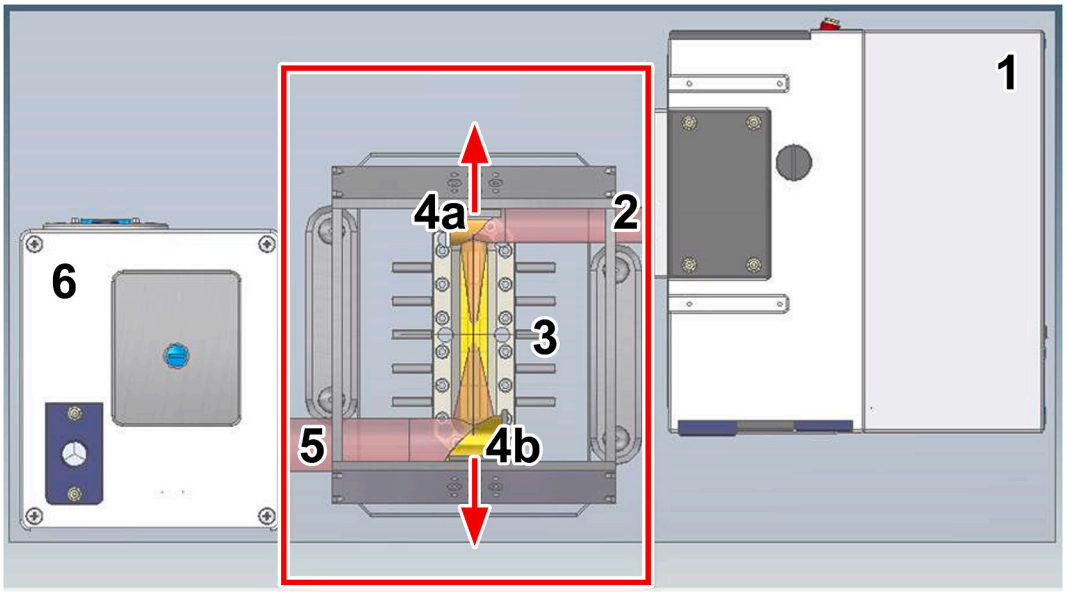

Fig. 3. Scheme of the DRIFTS Setup (top view). (1) Infrared-source, (2) IR-beam from spectrometer (3) reactor (4a) gold mirror (4b) gold mirror, (5) IR-beam to detector chamber, (6) detector chamber. Red rectangle: Encasement with Plexiglas®. (For interpretation of the references to colour in this figure legend, the reader is referred to the web version of this article.)

to subsequently subtract them from the absorbances of the catalyst, atmosphere, and instrument specifications according to Eq. (S1). In general, background and *operando* spectra were averaged over 40 spectra to obtain valid data for further analysis and to reduce background noise. After subtracting the background spectrum, a baseline correction was performed through concave rubberband correction. For all experiments not focusing on spatial resolution, but rather on variations of, e.g., SV, DRIFT spectra were recorded at the center of the last reaction zone (RZ5). For the spatially resolved DRIFTS experiments, background spectra were recorded at 5 mm intervals along the axial direction of the reactor. The exact position was set using a stepper motor to match the position of the background spectra as accurately as possible. For the spatially resolved investigations, further correction considering inhomogeneities in, e.g., catalyst layer thickness is considered in addition. Details are given in section 3.3.3.

All experiments were performed with a stoichiometric CO_2:H_2 ratio of 1:4 and 50 vol% N_2 at $p_R = 5$ bar(a). Experiments focusing on spatial resolution and variation of the space velocity (SV = 1–20 $ml_N\ mg^{-1}\ min^{-1}$ (= $60{\cdot}10^3$ – $1200{\cdot}10^3\ ml_N\ g^{-1}\ h^{-1}$), flow rate including N_2) were carried out at reaction temperatures of $T_R = 200$, 350 and 400 °C. The temperature resolved experiments were carried out at a constant SV of 4.6 $ml_N\ min^{-1}\ mg_{cat}^{-1}$ (= $276{\cdot}10^3\ ml_N\ g^{-1}\ h^{-1}$).

2.2. Computational fluid dynamics (CFD) model of the SRD reactor

2.2.1. Model and grid

Different authors used CFD (Computational Fluid Dynamics) simulations to investigate existing laboratory reactors, like Berty-type reactors [33], channel reactors [34,35] or fixed bed profile reactors [36]. The insight into the flow profile in the reactors and possible gradients can help to relate the experimental data to the results of numerical models. The CFD simulations offer the advantage of investigating reaction conditions in the reactor independently of experimental limitations and potential non-idealities. In addition to such insight, CFD simulations enable the identification of operating conditions that are particularly favorable and relevant for kinetic investigations, as has been demonstrated in recent literature [37]. The primary goal of the CFD simulations of the SRD reactor in this study is to deepen the understanding of flow effects in the reactor and to validate the sampling in general. The simulations for this investigation are based on the Finite Volume Method and are carried out using Ansys Fluent. Details on the mesh independence analysis (see Fig. S.9) and the implemented equations can be found in the supporting information.

The CAD (Computer Aided Design) model generated for the simulations represents the interior of the reaction chamber. The peripheries of the inlet and outlet regions are neglected, as are those of the gas sampling. For the inlet and outlet, only the slits where the fluid enters and leaves the reactor chamber are considered. These slits distribute the fluid evenly across the width of the reactor, which is crucial for establishing and maintaining a laminar flow field. For the gas sampling, only the initial pieces of the four sampling capillaries directly connected to the reaction chamber and located between the five microstructured foils are considered.

The generated volume mesh consists of a combination of mainly hexahedral cells in the free volume and polyhedral cells in the transition region near the wall. In addition, three thin boundary cell layers are inserted next to the reaction chamber walls. The characteristic cell length varies between a minimum and maximum value of $0.5 \bullet 10^{-4}$ m and $1 \bullet 10^{-4}$ m to ensure a sufficient resolution and a mesh independent solution.

Various operating conditions are investigated in steady-state simulations under isothermal conditions. While non-isothermal CFD-simulation can give further insight into temperature-dependent effects within the reactor, at the current state of investigation and based on the unique design of the reactor (see section 2.1.1) and supported by previous findings, the assumption of isothermicity is valid. The influence of the local relative pressure field on the density is omitted, and a pressure-based solver is used. Volume flow, temperature and pressure of the feed are varied according to the experimental conditions investigated. Variations in the inlet density due to changes in temperature and pressure are accounted for through the ideal gas law. In addition, the increase in density resulting from the net reduction in molar volume during the reaction is considered. For the investigation of the sampling procedure, a defined mass flow is deducted at different sample outlets for selected cases.

A Dirichlet boundary condition for the velocity is applied at the inlet and a Neumann condition for the pressure is applied at the main outlet at the end of the reactor. For gas sampling at the four sample outlets, the mass flow leaving the reactor through the capillary is set to a specific value if required and to 0 if sampling is not active. A no-slip condition is applied to the velocity at the walls.

2.2.2. Locally resolved fluid and residence time distribution

The distribution of the fluid in the reactor and the residence time are investigated numerically using Lagrangian particle tracking. A large number (≈ 13,000) of massless tracer particles are introduced at the inlet and tracked as they move through the flow field. These particles serve as tracers, i.e., they do not interact with the fluid and move through the reactor according to the calculated respective local flow field. The accessibility of the particle positions on their trajectories within the reactor allows a detailed analysis of the fluid distribution. To determine the residence time distribution, the particles and their residence time are tracked at the reactor and sample outlets. To analyze the flow regime in the reactor for different reaction conditions, a volume flow range from $\dot{V} = 450$–$1800\ ml_N\ min^{-1}$ and a temperature range from T = 250–450 °C was investigated.

2.2.3. Investigation of the gas sampling

Steady-state simulations are conducted with a second outlet at the tap. Again, Lagrangian particle tracking is used to determine which of the particles introduced at the reactor inlet leave the reactor at a sampling capillary. This allows to determine the probing zone within the reaction channel, i.e., which gas fraction of the reaction medium is actually sampled. To investigate possible occurring concentration gradients within the reactor, a reaction kinetic model is implemented using Ansys CHEMKIN for which the pre-implemented micro kinetic model published by Schmider et al. [5] is used. For details on the kinetic modeling, see supplementary Information. A so-called washcoat factor is introduced as multiplier for the surface reaction rates. This allows investigating reaction rates comparable to those observed in the conducted experiments without further adjustment of the kinetic model.

2.3. Alternative catalytic plate reactor for validation

2.3.1. Reactor set up and analytics

To validate the results of the catalytic reaction tests, the spatially resolved concentration profiles of the SRD reactor are compared with those of an established catalytic plate reactor (CPR) shown in Fig. 4. This plate reactor has already been extensively characterized and used for *operando* investigations on methanation reactions in several studies [11,15,28,29,34] and, thus, can serve as a reference to exclude, e.g., diffusion-limiting effects in the SRD reactor.

The catalytic plate reactor is an optically accessible channel reactor (dimensions 100 × 40 × 5 mm) in which a catalyst-coated stainless-steel plate is placed at the bottom (Fig. 4). In order to avoid any influence of the gas inlet, i.e. to allow for the formation of a laminar flow profile, the first part of the plate (10 mm) has not been coated with the catalyst [9,13,30], i.e. the dimensionless reactor length of “0.0” represents the actual beginning of the catalyst coating (for details on coating see section 2.3.2). The top is closed with a fused silica quartz window (Heraeus, TSC-3, Germany), which allows measurement of the catalyst

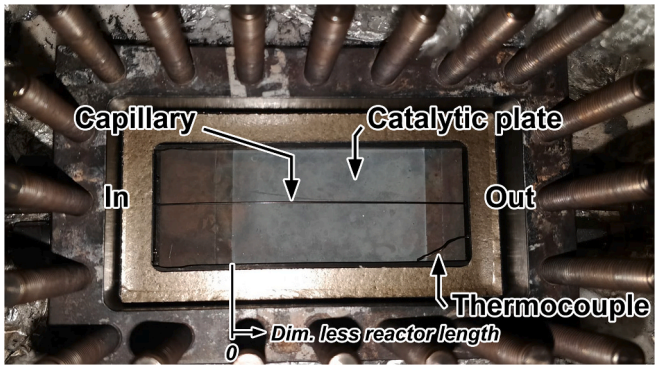

Fig. 4. Top view of the catalytic plate reactor with catalytic coated plate, thermocouple and capillary for gas sampling.

surface temperature profile using a shortwave infrared camera (FLIR, SC2500, Burlington, ON, Canada). To ensure a uniform temperature distribution, the channel is heated by six heating cartridges installed at the bottom beneath the catalyst plate. The reactants (CO_2, H_2, Ar as inert gas for dilution) are fed via calibrated mass flow controllers (red-y smart Vögtlin) and enter the reactor from the left side, flow over the catalyst-coated plate and exit on the right side. A movable stainless-steel capillary (SS316, 0.5 mm outer diameter) is inserted from the right side, enabling spatially resolved measurement of the gas composition above the coated catalyst using a calibrated quadrupole mass spectrometer (Hiden Analytical, HPR-20, UK). Tests confirmed that the capillary, as well as the uncoated metal plate, are not active towards the CO_2 methanation. In addition, CFD modeling confirmed that the reactor is ideally suited to collect kinetic data, and the capillary does not falsify the kinetic data [11,15,28,29,34]. For the current study, the step motor moves every 4 mm, resulting in 18 data points along the length of the catalyst zone.

2.3.2. *Experimental procedure*

For the comparison between the SRD and the CPR, a nickel-manganese spinel catalyst described in [38] was used. Frame coating was used to deposit the catalyst slurry onto the stainless steel plate [15,28]. The slurry preparation involves mixing isopropanol (99.5 %, Fisher, Canada) with a binder (Disperal P2, Sasol) under constant stirring (≈1000 RPM) for 1 h. Then the catalyst was added in a catalyst-to-binder mass ratio of 9:1 and stirred for an additional hour. A rectangular steel frame was fixed on top of the stainless-steel plate and levelled. Then, approximately 1.5 ml of slurry was poured into the framed area. After the isopropanol had evaporated (ambient air), the coated plate was calcined at 450 °C for 1 h in a muffle furnace with a heating rate of 2 K min^{-1}. To ensure that the catalyst was uniformly coated on the plate, the coating height over the plate was determined by profilometry (Dektak XT, Bruker, USA). The size of the coated area was 64 mm × 48 mm and had an average height of 22 μm. The coated catalyst plate was then installed in the catalytic plate reactor and reduced in 10 vol% hydrogen in argon at 450 °C for 1 h. Details on the operating parameters for the intended comparison between SRD and CPR are given in 3.1.

3. Results

3.1. *Validation of the SRD reactor by the reference CPR*

To assess the reliability of the gas-phase data obtained from the SRD reactor, the methanation reaction was performed under the same experimental conditions in both the SRD reactor and the well-established CPR. The reactions were carried out at 400 °C, 5 bar(a), a SV of 4.6 $ml_N\ min^{-1}\ mg_{cat}^{-1}$, a stoichiometric feed ratio of CO_2 to H_2 of 1:4 and 50 vol% dilution with inert gas. Since the CPR is connected to an MS, here, Ar was used for dilution while N_2 was used for the SRD reactor. Besides the different concepts for gas sampling (SRD reactor: 6 dedicated sampling ports vs. CPR: 18 points due to the applied step width of 4 mm), the applied analytics also differ in different metrics: The MS of the CPR is rather fast but has a higher relative error at very low concentrations as compared to the GC used for the SRD reactor which in return requires longer analysis time.

The spatially resolved concentration and derived conversion profiles are shown in Fig. 5. Since both reactors have different reaction zone lengths, the dimensionless reactor length was used for the comparison. Differences in the number of data points are due to the different concepts of gas sampling. The comparison of the concentration profiles over the reactor length of the two reactors shows very similar progression of the gas phase concentrations along the catalyst layer, i.e., dimensionless reactor length. It should be emphasized that the catalyst coatings applied in the two reactors for practical reasons do show some non-ideal distribution along the dimensionless reactor coordinate. However, the feed flow rate was precisely adjusted to the total catalyst mass to achieve 4.6 $ml_N\ min^{-1}\ mg_{cat}^{-1}$ in both cases. The observed deviation between the two reactors (maximum deviation at a dimensionless reactor length of ≈0.2), can be explained by the non-ideal catalyst distribution having a disproportionate influence especially at high reaction rate, i.e. at the beginning of the reactor (between a dimension less reactor length of 0.0 and 0.4). At the end of the reactor, the CPR achieved a CO_2 conversion of 72.0 %, while the SRD reactor achieved 75.5 %, resulting in a difference of only 3.5 percentage points. CO is present at a concentration of less than 0.5 vol% at max (SRD reactor), which was below the detection limit of the MS. Therefore, the resulting CH_4 selectivity only match in the

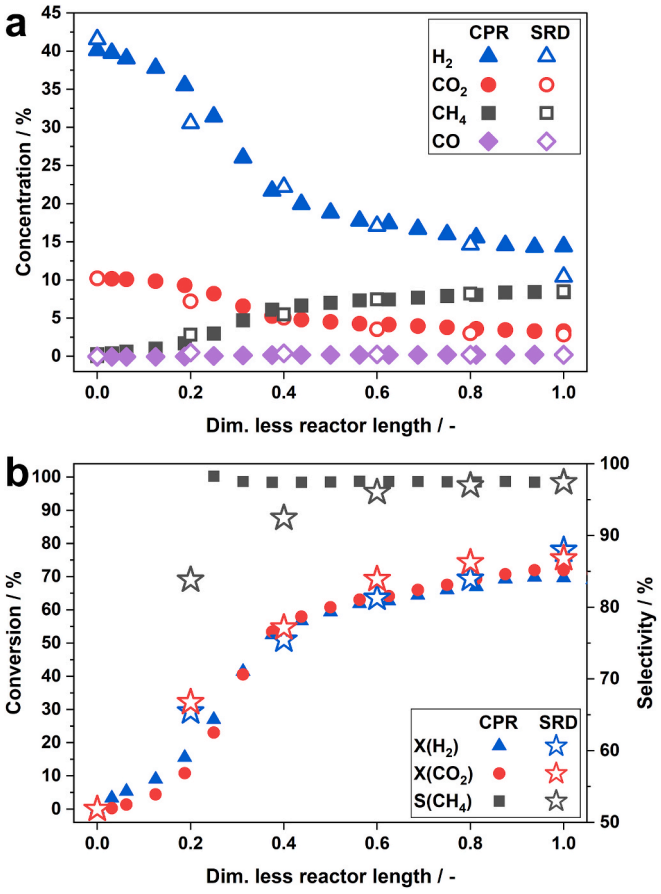

Fig. 5. Comparison of the CPR with the SRD reactor. (a) Concentration of various gas phase species and (b) conversion and selectivity as a function of the dimensionless reactor length. All data at 400 °C, 5 bar(a), SV = 4.6 $ml_N\ min^{-1}\ mg_{cat}^{-1}$, 50 vol% N_2(SRD)/Ar(CPR), CO_2:H_2 = 1:4. Full symbols: CPR, empty symbols: SRD reactor.

downstream half of the reaction zones where the CH_4 concentration is high and, thus, selectivity is not that much falsified by the missing CO concentration data in the case of CPR experiments. Here, the values obtained compare well with previously published simulation results [22] as well as with reaction data of the very same catalyst [23,24]. Conversion and selectivity profiles at temperatures of 250, 300, 350 and 450 °C (see Fig. S.1) show similar trends. The observed very good agreement between the two reactors is of particular importance as it validates the accuracy of the SRD reactor and thus the results discussed later.

3.2. CFD simulation

3.2.1. Flow characterization of SRD reactor

To determine the appropriate level of detail needed to accurately model the SRD reactor, a thorough understanding of the flow regime within the reactor is essential. Furthermore, to use the measured data in the parametrization of kinetic models, it needs to be verified that the experimental data points are reliable.

The results of the CFD simulations are depicted in Fig. 6. The investigation of the flow field at the reactor inlet is particularly important because potential backflows or stagnant zones can significantly influence the residence time within the reactor. In Fig. 6a, the gas velocity at the reactor inlet is shown in side view at different positions at the reactor width. It can be seen that the velocity profile is almost identical for all positions. In Fig. 6b, the flow streamlines are shown, indicating that the laminar flow is reached almost immediately behind the reactor inlet and before the first catalyst plate. A fraction of the entering gas is deflected by the reactor window at the top and flows back into the stagnant zone behind the reactor inlet. Nevertheless, this fraction is negligible compared to the main flow of the gas. The flow field in the whole reactor is depicted in Fig. 6c. The flow field consists of parallel streamlines with low mixing in direction of the width of the reactor.

Considering the simulation results, the flow field within the reactor is strongly laminar with low mixing in direction of channel height and width. To further investigate these findings, the residence time distribution is calculated for different operating conditions.

3.2.2. Residence time distribution

The cumulative residence time distribution for the reactor with different simulation conditions is shown in Fig. 7. The first tracer particles leave the reactor at normalized residence times $\Theta \approx 0.67$, which represents the fastest flow in the center of the reaction channel. The curve then asymptotically approaches 1, which is a typical characteristic of laminar flows [39]. The results for the volume flow variation (Fig. 7a) indicate that the residence time distribution is dependent on the volume flow in the reaction channel. Still, even for maximal flow rates of 1800 $ml_N\ min^{-1}$, the behavior of the reactor is close to an ideal laminar flow channel reactor (LFCR). For moderate volume flows, the curves are between the ideal laminar flow tubular reactor (LFTR) and the channel flow reactor. The temperature dependency of the residence time distribution (Fig. 7b) is negligible. As consequence, the same reactor model can be used over the whole temperature range.

3.2.3. Validation of gas sampling

The fraction of tracer molecules that are sampled at the probing tap is shown for the simulation at reference conditions (400 °C, 5 bar, 530 $ml_{STP}\ min^{-1}$) in Fig. 8.

It is clearly visible that the area of the sampling is locally strongly focused, especially regarding the reactor width. In combination with the low mass transport due to the laminar flow regime, these findings indicate that concentration gradients in the reaction channel need to be excluded to guarantee the validity and representativeness of the gas phase compositions which were taken at the probing taps.

The molar fractions over the fifth catalyst plate along the reaction chamber height and width are presented in Fig. 9 for a simulation at reference conditions (400 °C, 5 bar, 530 $ml_N\ min^{-1}$). The wash coat factor was modified to reach a moderate CO_2 conversion of

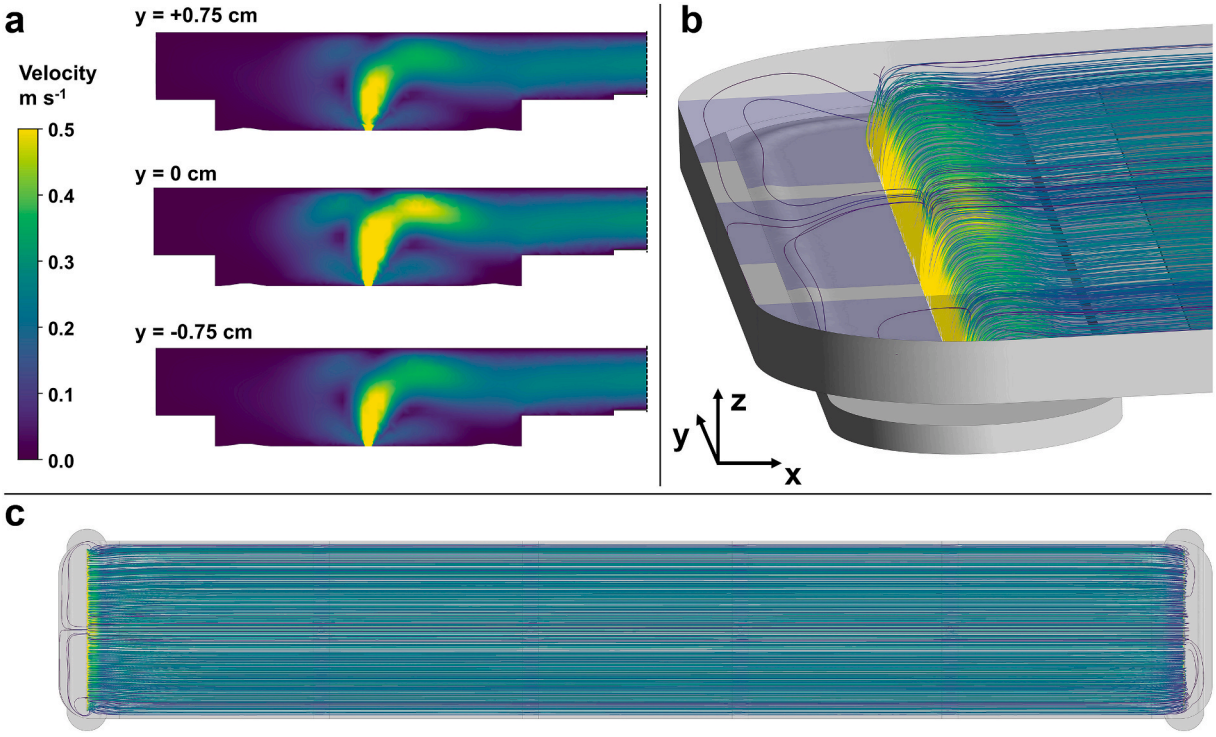

Fig. 6. Results for the CFD simulation of the inlet of the SRD reactor. (a) Side view of the velocity field at the reactor inlet. (b) Streamlines at the reactor inlet. The positions of the contour plots from (a) are indicated as blue shaded planes. (c) The flow field through the whole reactor. Simulation parameters: $\dot{V}_{in} = 530\ ml_N\ min^{-1}$, T = 400 °C, p = 5 bar. (For interpretation of the references to colour in this figure legend, the reader is referred to the web version of this article.)

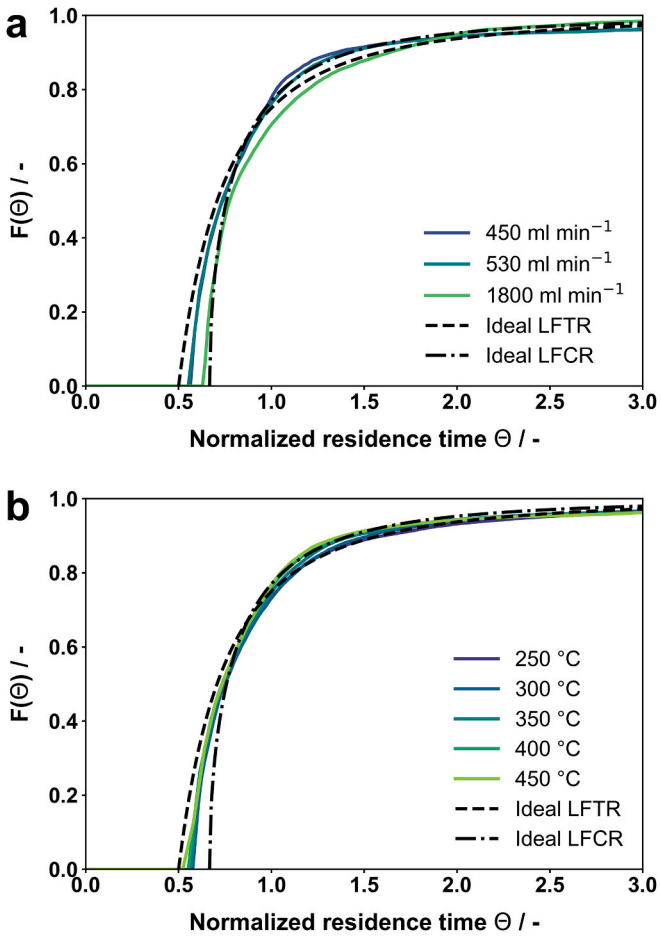

Fig. 7. Residence time sum function generated from the CFD data. (a) Volume flow variation with constant temperature T = 400 °C. (b) Temperature variation with constant volume flow $\dot{V}$ = 530 ml_N/min. In both cases, the SRD reactor lies between the ideal laminar flow (tubular) reactor (LFTR) and the ideal laminar flow channel reactor (LFCR).

approximately 40 %, which is a typical value for kinetic experiments in the SRD reactor. The concentration gradients show the expected behavior. The molar fractions of the reactants are the lowest at the catalyst surface and increase towards the top of the reaction chamber, while the products show the opposite trend. The byproduct CO is only present in negligible amounts with almost no gradients. The molar fraction of nitrogen increases slightly towards the catalyst layer because of the reduction of the number of moles during the reaction. The relative concentration deviation between the catalyst surface (h = 0) and the top of the reaction channel (h = 1) is 2.61 % for the molar fraction of CO_2 and 0.72 % for H_2. The relative gradient for H_2 is smaller, because the diffusivity and the absolute concentration is higher. At the outer reactor boundaries in direction of width, the conversion is slightly increased, resulting in higher product and reduced reactant concentrations. This effect can be assigned to the lower gas velocities, and, thus increased residence time due to boundary effects. Overall, the gradients in the direction of reactor width and height are small compared to the gradients in axial direction, and therefore negligible.

In Fig. 10, the averaged conversions of CO_2 and H_2 and the conversions in the sampling zones are presented. While the mean absolute percentage error is rather small (X_{CO2}: 2.3 %, X_{H2}: 1.9 %, S_{CH4}: 0.2 %), some trends can be identified: The deviation of CO_2 is slightly higher in comparison to H_2, since the diffusivity of CO_2 in the reaction channel is lower. Furthermore, the conversions are underestimated in the sampling zones compared to the average over the whole reactor cross section. As already discussed, the reason for this is the higher conversion in the boundary area of the reaction channel, which are not covered by the sampling. Nevertheless, the deviation is only minimal and in the range of typical experimental error.

In conclusion, the results of the simulation studies indicate that the SRD reactor can be approximated as an ideal laminar flow channel reactor. Furthermore, in the CFD simulations, the sampling taps accurately represent the local gas-phase composition within the reactor. This demonstrates the validity of the experimental sampling procedure applied, thereby providing a reliable basis for kinetic modeling.

3.3. Investigation of the CO_2 methanation reaction using operando DRIFTS

3.3.1. Temperature-dependency of the adsorbed and gas phase species in methanation reaction

Temperature-resolved DRIFT spectra were recorded in the range of 100–450 °C. The corresponding spectra are shown in Fig. 11a: Most of the species are visible already at the starting temperature of 100 °C. The bands in the range of 2100–1800 cm^{-1} originate from adsorbed carbonyls, which are bound to the nickel. In particular, the band at a wavenumber of about 2062 cm^{-1} can be assigned to nickel centers bound to three linearly bound carbonyls (Ni–$(CO)_3$), while nickel linearly bound to two carbonyls (Ni–$(CO)_2$) corresponds to the band at a wavenumber of 2044 cm^{-1}, and nickel with one single linear or bridged CO can be assigned to the band at 2011 cm^{-1} (Ni-CO) and 1917 cm^{-1} (Ni═CO), respectively [40]. The bands of multi-bond carbonyls vanish almost completely until 300 °C, which is why these species are not further analyzed in detail. Adsorbed bicarbonate (*HCO_3^-) results in bands at 1649, 1440 and 1230 cm^{-1}, adsorbed formate (*$HCOO^-$) causes bands at 2900, 1587, 1394 and 1373 cm^{-1} [40–48], due to the individual rotations and vibrations. To derive meaningful trends for the corresponding surface concentrations, the absorbance values derived for each species within this set of spectra were normalized to the maximum absorbance (see Eq. (S2)). Fig. 11b shows the normalized absorbance of

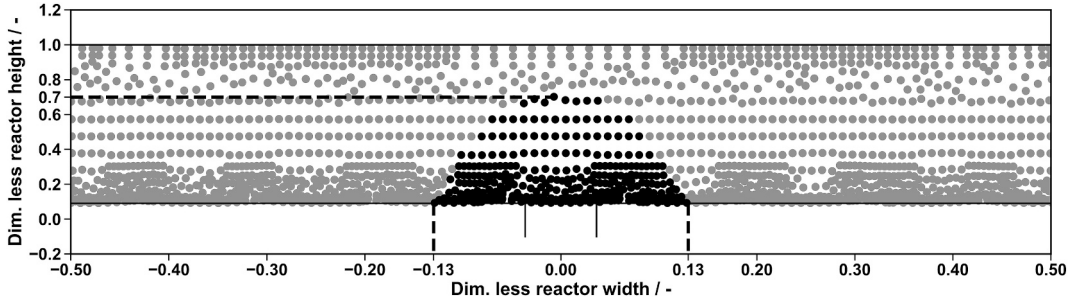

Fig. 8. Cutout of the cross section of the reaction channel. The dots represent tracer particles in the CFD simulation. The black lines indicate the boundaries of the reactor, including the probing capillary. The black highlighted particles are the particles that leave the reactor at the probe outlet. While the probing zone covers approx. 70 % of the channel height, only approx. 13 % of the reactor width is covered.

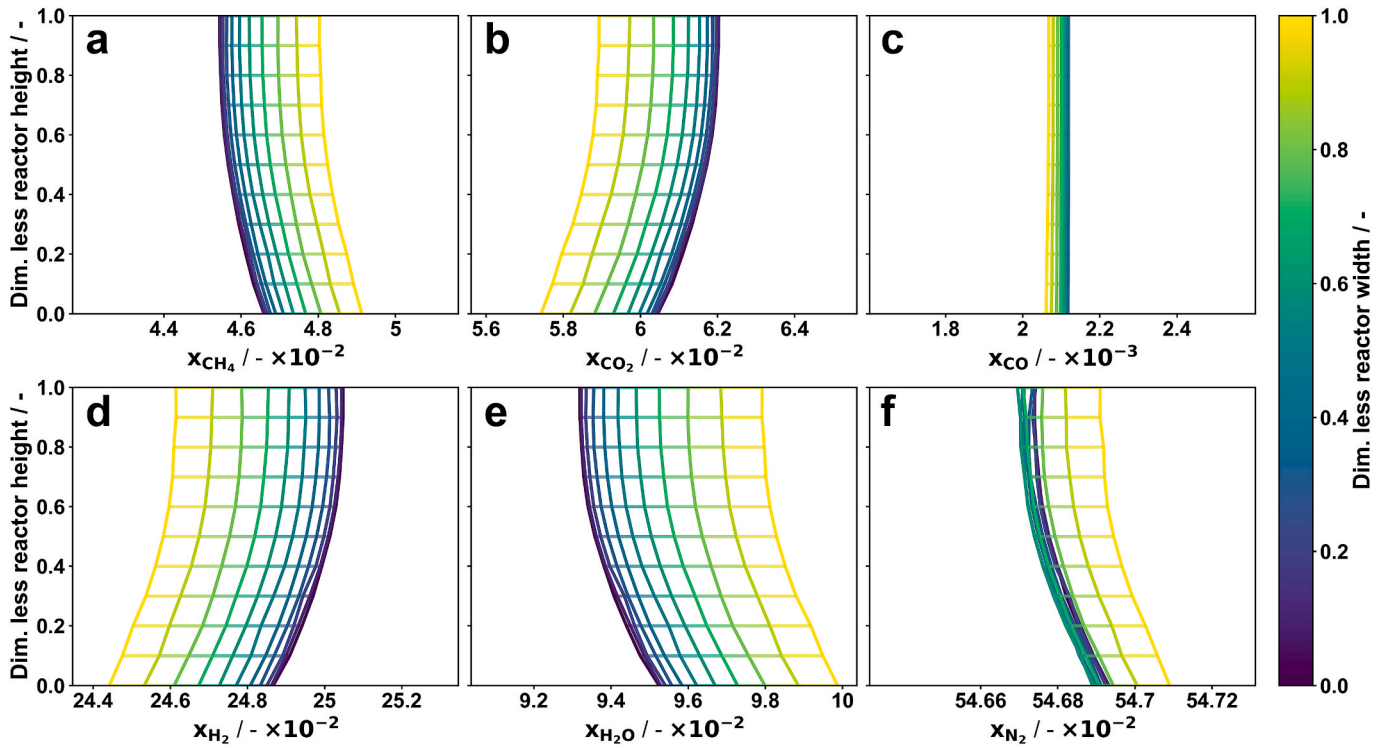

Fig. 9. Concentration within the reaction channel at the fifth catalyst plate. The plots for CH_4, CO_2, H_2 and H_2O are scaled such that the x-axis limits represent the average concentration +/− 0.05. For CO and N_2, the axis limits are x_{mean} +/− 0.005.

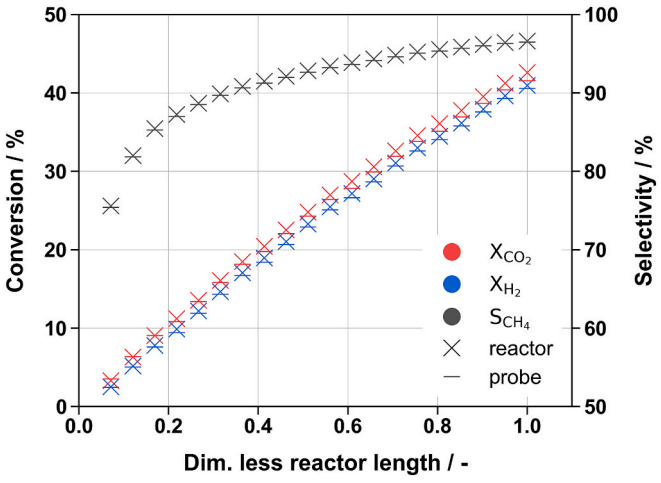

Fig. 10. Calculated conversion and selectivity over the whole reaction channel and at the area of the gas sampling at different axial coordinates for the reference case (400 °C, 5 bar, 530 ml_N min^{-1}).

bicarbonate, formate, Ni–CO and CH_4 as a function of temperature derived from the temperature-resolved spectra. As the reaction temperature is increased, the bands of multi-bond carbonyls Ni–$(CO)_2$ and Ni–$(CO)_3$ decrease and only the Ni–CO and Ni═CO bands remain constant at temperatures above 250 °C. Bicarbonate is mainly adsorbed on the catalyst surface at low temperatures. As the temperature increases, the absorbance and, therefore, the surface concentration decrease. Even at low temperatures, bicarbonate reacts to formate (path III in Fig. 1), which is why the surface concentration of formate readily increases with temperature up to approx. 175 °C. Once the bicarbonate bands are no longer detectable, the concentration of formate starts also to decrease with further increase in temperature as formate most likely continues to react faster to adsorbed carbonyl species (path IV in Fig. 1) than it is formed from bicarbonate. This trend was also found by Cárdenas-Arenas et al. [49] for a Ni/Al_2O_3 catalyst. In parallel to reaching the maximum of formate absorbance (175 °C), the band which can be assigned to CH_4 in the gas phase is first detected (at approx. 200 °C) and further continuously increases in its absorbance value up to the maximum temperature investigated (450 °C) while the absorbance of the formate band decreases. This is due to the fact that with increasing reaction temperature formate formation is not that much accelerated as its conversion to CO, or eventually CH_4. As a side note, the increase in normalized CH_4 concentration perfectly matches with the GC data (see Fig. S.2). The disappearance of bicarbonate with a simultaneous increase in formate concentration suggests that the latter is instantly formed by bicarbonate. Ni–CO shows a slow increase in concentration over the whole temperature range, since it can be formed by dissociation of CO_2* and of formate (paths I and IV, respectively in Fig. 1) [50]. From 250 °C, the Ni–CO concentration remains rather constant before it decreases again with further increasing temperatures starting at approx. 425–450 °C. This suggests that the nickel centers with three (Ni(–$CO)_3$) and two (Ni(–$CO)_2$) bond carbonyls are restructured to eventually single bond linear nickel, which qualitatively can also be observed in the temperature resolved spectra (Fig. 11a). In addition, the carbonyl may be formed by dissociation of formate (path IV in Fig. 1), which also explains the decrease in formate concentration starting from 200 °C and was also found by Kumar et al. [51]. The CO_2 conversion was 64.5 % at 450 °C, where it slowly approaches equilibrium conversion. To validate the collected DRIFTS data, a second DRIFTS experiment has been carried out under the exact same reaction conditions but with a new batch of catalyst (see Fig. S.7 in the supplementary). It can clearly be seen that the trends from the adsorbed species as well as the gas phase species such as CH_4 follow the same trends in both experiments. The DRIFTS experiment was concluded within a period of 24 h in which no noticeable catalyst deactivation occurred (see Fig. S.8 in the supplementary).

3.3.2. *Influence of space velocity on adsorbed and gas phase species*

In order to assess the influence of space velocity, SV-variation was

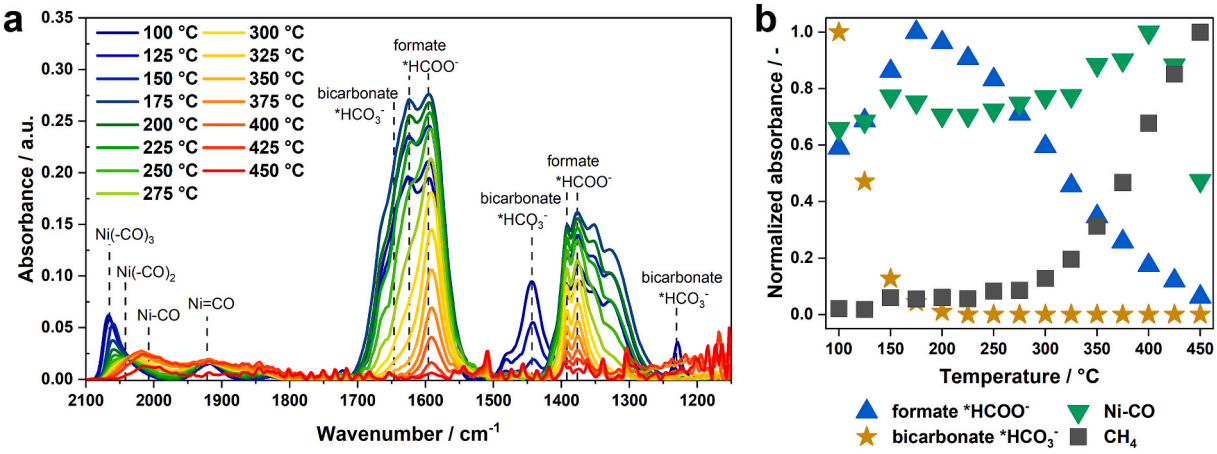

Fig. 11. (a) DRIFT spectrum of the methanation reaction at different temperatures at 5 bar(a), SV = 4.6 $ml_N\ min^{-1}\ mg_{cat}^{-1}$, 50 vol% N_2, CO_2:H_2 = 1:4, in RZ5. (b) Normalized peak heights for formate (1373 cm^{-1}), Ni-CO (2011 cm^{-1}), bicarbonate (1448 cm^{-1}), CH_4 (3003 cm^{-1}) as a function of the reaction temperature.

followed using operando DRIFTS and online GC at two distinct reaction temperatures (350 °C and 400 °C). Fig. 12 shows the normalized absorbance of the gas phase reactant CO_2, the adsorbed intermediates formate and Ni–CO as well as the resulting gaseous CH_4 determined by DRIFTS at the center of the rearmost catalyst plate. Relative CO concentration was determined by GC at the reactor outlet due to its very low concentration <0.2 vol% (350 °C) and <0.5 vol% (400 °C) which could not be resolved by DRIFTS. As to be expected, the maximum CO_2 conversion (50 % at 350 °C and 80 % at 400 °C) was obtained at the lowest SV investigated, i.e. SV = 1 $ml_N\ min^{-1}\ mg_{cat}^{-1}$, but did not reach the thermodynamic equilibrium (93 % at 350 °C and 88 % at 400 °C). Therefore, when further increasing the SV, the CO_2 outlet concentration also increases while the methane concentration decreases. The surface concentration of formate does well correlate to the gas-phase concentration of CO_2, underlying that its formation directly depends on the concentration (i.e. partial pressure) of CO_2 in the gas phase. Interestingly, at 400 °C, the surface concentration of formate first decreases with increasing SV (from SV = 1–3 $ml_N\ min^{-1}\ mg_{cat}^{-1}$, see Fig. 12b) before it increases again with further increase in SV, while CO_2 gas phase concentration steadily increases. In this region of low SV, in contrast to 350 °C where Ni-CO surface concentration is rather constant, for 400 °C the normalized Ni–CO absorbance strongly increases with SV, indicating that Ni–CO is formed from formate (path IV in Fig. 1) being initially also formed via an intermediate bicarbonate (path III in Fig. 1). Besides, the decrease of Ni-CO surface concentration with decreasing SV also directly correlates with CH_4 formation, which is more pronounced at 400 °C as compared to 350 °C. The nearly SV-independency of the normalized absorbance of Ni-CO at 350 °C can be assigned to the fact that Ni–CO is already present on the catalyst surface in very small amounts (see Fig. S.3 for absolute absorbance values) and reacts very quickly to methane. At 400 °C, the Ni–CO surface concentration decreases at very high conversion rates resp. low SV because the CO_2 concentration decreases and, thus, most likely also Ni–CO formation via path I in Fig. 1. These findings suggest that while the dissociation of Ni-CO to C* and O* is the rate-determining step (being in line with literature, e.g. Ref. [52]), the formation of Ni-CO decreases at high conversion rates relative to the dissociation of Ni-CO. In addition to the reactants and adsorbed species determined via DRIFTS, Fig. 12 also shows the normalized concentration of gaseous CO as a function of SV from GC analysis. Here, especially for 400 °C, the normalized CO concentration follows the trend of Ni–CO, indicating that gaseous CO is mainly formed via Ni–CO which was also found be Franken et al. [48]. However, it is worth mentioning that the absolute concentration of gas phase CO is rather low (<0.5 vol% in all cases, see figure S.3).

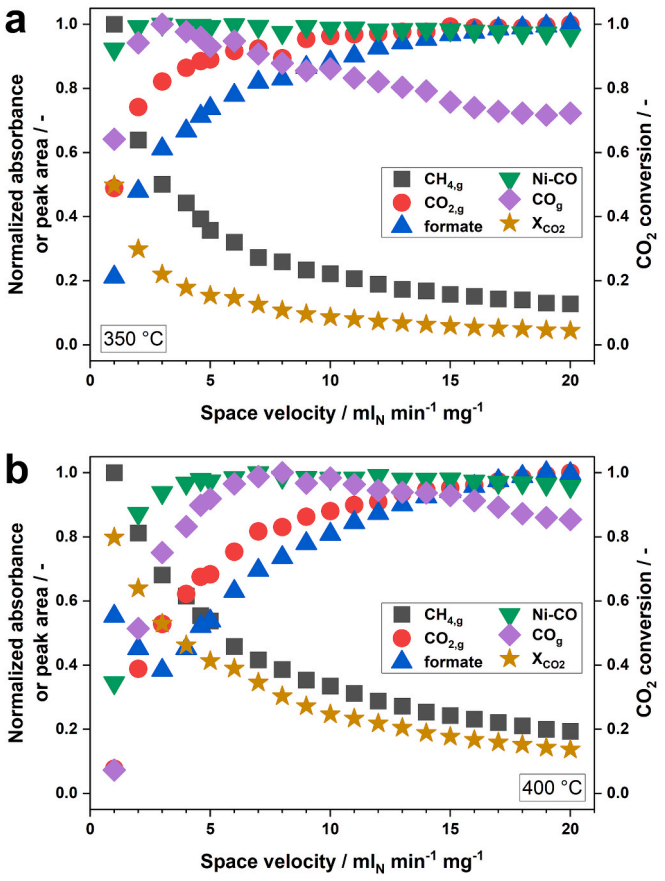

Fig. 12. Normalized peak heights of formate (1600 cm^{-1}), Ni-CO (2011 cm^{-1}), $CO_{2,g}$ (2364 cm^{-1}), CH_4 (3003 cm^{-1}), CO_g (GC) and CO_2 conversion (GC) plotted over the SV at a reaction temperature of (a) 350 °C and (b) 400 °C, at 5 bar(a), 50 vol% N_2, CO_2:H_2 = 1:4, in RZ5.

3.3.3. *Investigation of CO_2 methanation reaction in spatial resolution*

In the above, SV was varied by adjusting the volumetric inlet flow rate. The SRD reactor shown also allows monitoring of the adsorbed species along the reactor length, which in turn causes a variation in SV without changing the volumetric inlet flow rate, thus providing valuable insights into the reaction mechanism.

However, as DRIFTS is quite sensitive to the catalyst layer properties (e.g. layer thickness, homogeneity), for reliable DRIFTS investigations comparing different positions the subtraction of background spectra correcting equipment and material effects (see section 2.1.3) must be

accompanied with corrections considering the properties of the catalyst at the very position investigated along the reactor coordinate. Thus, reference spectra at a low reaction temperature (i.e. negligible methanation reaction) must be included in addition to the subtraction of the background spectra. Here, reaction conditions are mandatory to identify the reaction species and compare them at different positions in the reactor. For this purpose, locally resolved spectra were recorded at 200 °C, since at these low temperatures basically no conversion of the reactants takes place (see section 3.3.1) and therefore the same conditions prevail throughout the gas phase along the reactor coordinate. These reference spectra are shown in Fig. S.4. Preliminary tests have shown that only the adsorbed species on the catalyst are affected by the local changes of the catalyst layer, so only these are considered in the reference spectra. The locally resolved spectra (after background correction) of the adsorbed species at reaction temperatures of 350 and 400 °C are shown in Figs. S.5 and S.6, respectively. By dividing the absolute absorbances at each position to be analyzed by the absorbances of the accordant reference spectrum (see Eq. (S4)), the influences of the catalyst surface on the signal are eliminated, so that only the dependence of the position along the reactor coordinate on the adsorbed species can be revealed. Further, the relative absorbance values obtained were further normalized to the maximum relative absorbance of the individual species (Eq. (S5)) and plotted over the dimensionless reactor length, see Fig. 13a for 350 °C and Fig. 13b for 400 °C, both at a pressure of 5 bar(a), a SV of 4.6 $ml_N\ min^{-1}\ mg_{cat}^{-1}$ and a stoichiometric feed ratio of CO_2 to H_2 of 1:4 at 50 vol% dilution with N_2. The CO_2 conversion (GC-based) at the end of the reactor reaches 12 % at 350 °C and 36 % at 400 °C, respectively. From DRIFTS data, the decrease in gaseous CO_2 concentration is barely noticeable at 350 °C, but is clearly visible at 400 °C. While the CO_2 concentration decreases over the length of the reactor, the CH_4 concentration increases continuously. As the gas phase concentrations change, the adsorbed species also change: At 350 °C, the formate species decrease continuously along the reactor coordinate, which is related to the decrease in $CO_{2,g}$ and is also visible at 400 °C. The Ni–CO species is only present on the catalyst in low concentration (see spectra, Fig. S5) and does barely vary over the length of the reactor at 350 °C which is also found by Sichert et al. [50] for a Ni/Al_2O_3 catalyst. This indicates that at this temperature, the rate of Ni-CO formation (paths I and IV in Fig. 1) and its further reaction to CH_x are somewhat identical and independent of the reactor coordinate. At 400 °C, an increase in the normalized absorbance of Ni–CO over the reactor length can be observed. However, since the absorbance and therefore the concentration is very low (see spectra, Fig. S6), there is not much variation in absolute numbers compared to other species. At the temperatures of 350 and 400 °C the conversion is high enough to see relevant gradients in the spatial resolution and at the same time low enough to distinguish the different species in the DRIFT spectrum.

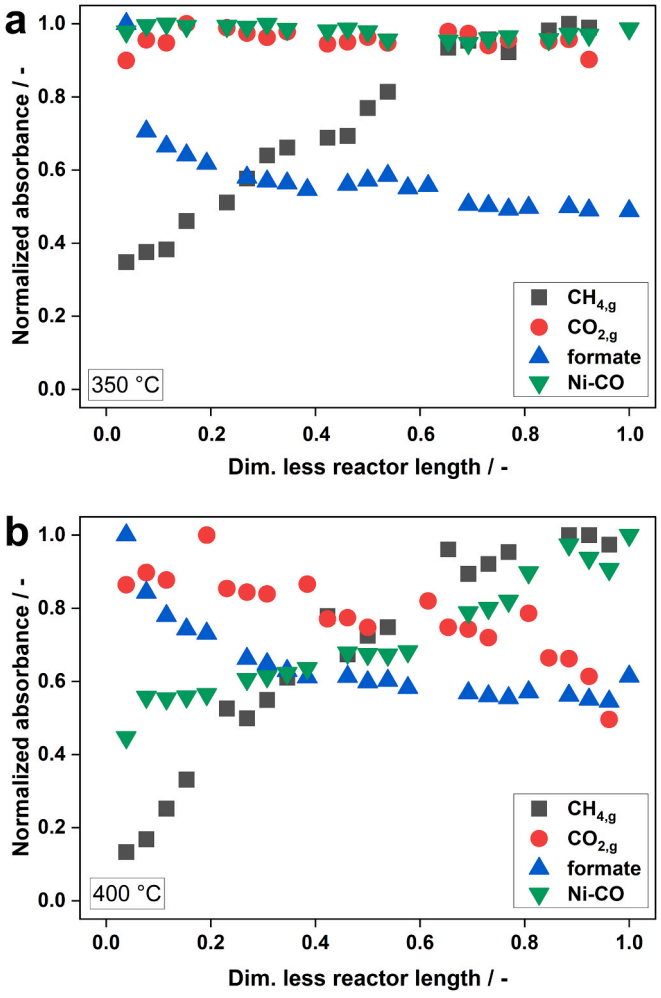

Fig. 13. Normalized peak heights of formate (1600 cm^{-1}), Ni-CO (2011 cm^{-1}), $CO_{2,g}$ (2364 cm^{-1}) and CH_4 (3003 cm^{-1}) plotted over the dimensionless reactor length at a reaction temperature of a) 350 °C and b) 400 °C, at 5 bar(a), 50 vol% N_2, CO_2:H_2 = 1:4, SV = 4.6 $ml_N\ min^{-1}\ mg_{cat}^{-1}$, in RZ5.

The values obtained from the spatially resolved analysis correspond to a reciprocal SV variation (see also Supporting Information, Fig. S9), however, without changing the total volumetric flow rate and, thus, without changing the flow conditions within the reactor. Fig. 14 shows the comparison of the normalized absorbance values from SV-variation (section 3.3.2) to the ones obtained from the spatially resolved measurements calculated based on the catalyst mass of the individual reaction zones for the gas phase species at 350 and 400 °C (a and b) and for the adsorbed species (c and d).

At 350 °C, the normalized absorbances of the gas phase and adsorbed species match well. Small deviations can be observed for the methane absorbances. At the higher temperature of 400 °C, the infrared signal in general is getting weaker and, thus, harder to evaluate resulting in a higher deviation between the experiments with spatial resolution and SV variation. However, the gas phase species again match quite well while the adsorbed species show a higher deviation due to the low amount of absorbance, especially for the Ni-CO component. The CO_2 conversion calculated from GC measurements during SV variation and spatially resolved measurement at 350 and 400 °C (Fig. 14e and f respectively) show a good fit with deviations of less than 20 %. These small variations can be assigned to the time difference of 24 h between the measurements. The spatially resolved gas phase measurements were taken directly after reduction while the catalyst still gained some activity. However, in general, using the spatially resolved measurements allows for fast and reliable collection of DRIFT spectra which correlate especially at lower temperatures well with data obtained from the SV-variation achieved by changing the volume flow.

4. Summary and conclusion

In this contribution, a dedicated spatially resolved DRIFTS (SRD) reactor setup, is presented. Gas sampling between five individual catalyst zones (applied as coated layers) in combination with *operando* DRIFTS at variable positions along the reactor coordinate allowed for highly spatially resolved profiles of the gas phase concentrations and adsorbed species on the catalyst surface. Aiming to gather meaningful insights in the occurrence and development of adsorbed species along the reactor coordinate, an approach for semi-quantification of the DRIFT-spectra is presented as well. Results from reactor modeling in combination with a reaction kinetic model from literature, and further the corresponding flow field obtained by CFD simulations revealed that the SRD reactor can be approximated as an ideal laminar flow channel reactor with only small gradients along the channel height. Thus, the

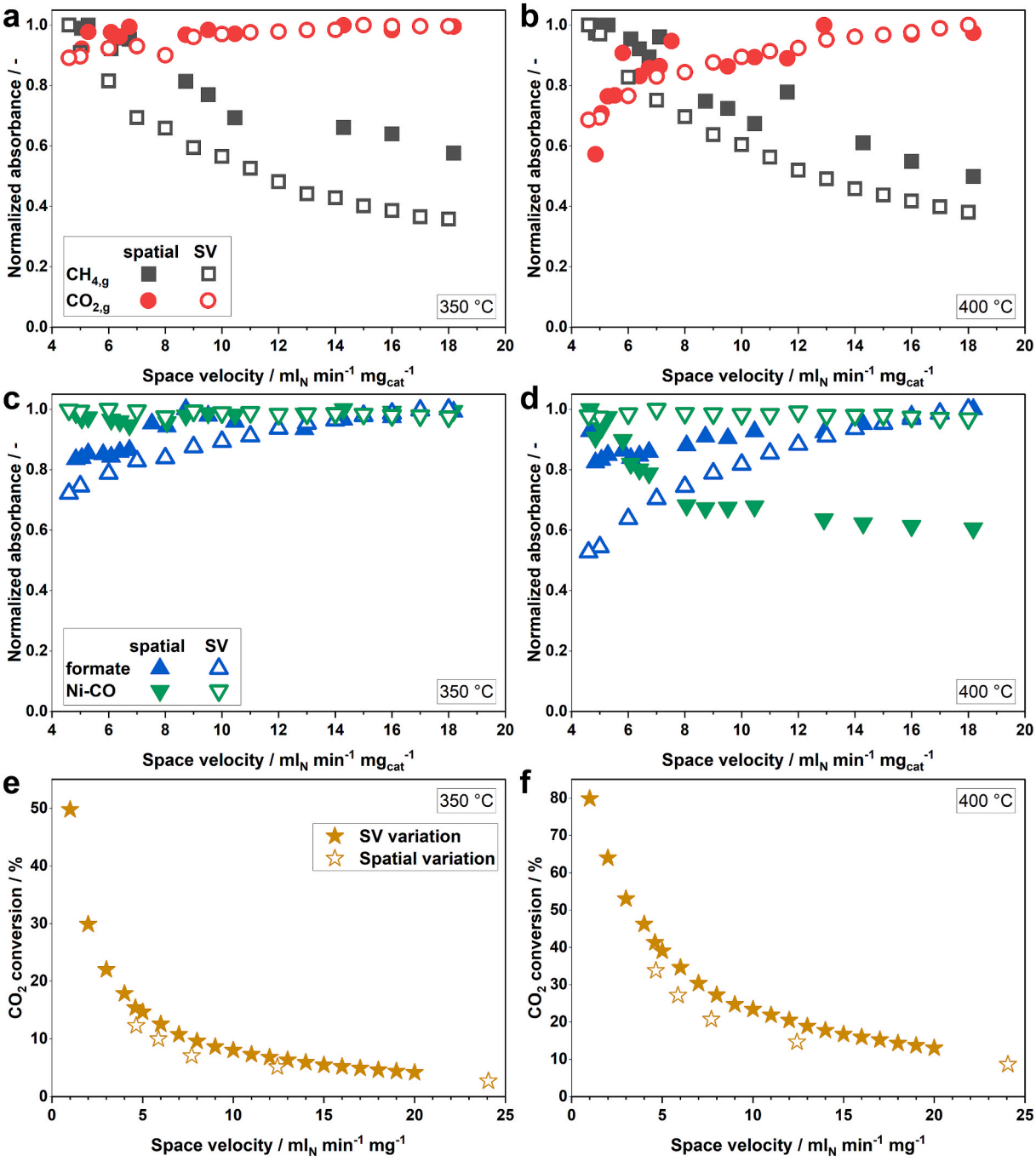

Fig. 14. Comparison of the normalized absorbances from SV variation to data obtained from spatially resolved analysis for (a) the gas phase species at 350 °C, (b) the gas phase species at 400 °C, (c) the adsorbed species at 350 °C, (d) the adsorbed species at 400 °C, and the resulting CO_2 conversions at (e) 350 °C and (f) 400 °C.

experimentally applied sampling concept provides an accurate representation of the actual concentration at the reactor coordinate of interest. The data obtained from the SRD reactor was used to unravel the influence of reaction temperature and space velocity on the methanation reaction over an industrial Ni/Al_2O_3 methanation catalyst. The validity of the results (gas phase analysis) obtained was experimentally proven by benchmarking the concentration profiles of the SRD reactor to a well-characterized catalytic plate reactor with the same catalyst and process conditions applied.

The main reaction pathway identified based on the operando investigations is summarized in Fig. 15. In particular, the operando results obtained suggest that with increasing reaction temperature (100 °C to 175 °C) bicarbonates readily react to formate (path III in Fig. 15) which, together with the subsequent intermediate product Ni–CO, is the most important detectable intermediate in the methanation reaction as CO* is one of the species needed for methane formation and as in present study Ni-CO* could be correlated with CO_2 conversion. With further increase in temperature, formate coverage starts to decrease accompanied by further formation of adsorbed carbonyl species and eventually the formation of methane starting at approx. 200 °C. The Ni–CO concentration only decreases from 425 °C onward, at which point the thermodynamic equilibrium is approximated.

Besides, space velocity variation (which also varies the conversion) confirmed the direct dependency of formate coverage with CO_2 concentration in the gas phase. At 400 °C and in the low SV region, Ni-CO coverage strongly increases while formate coverage decreases with SV,

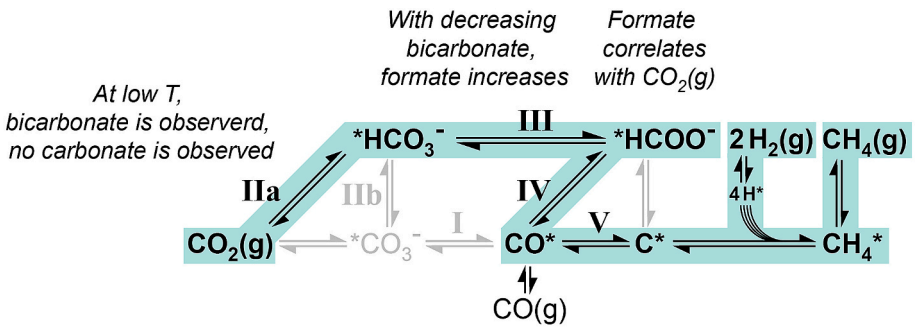

Fig. 15. CO_2 methanation reaction on the industrial Ni/Al_2O_3 catalyst: main reaction pathway (highlighted) identified based on the operando analysis.

indicating that Ni-CO is mainly formed from formate (path IV in Fig. 15) originating from bicarbonate species. This is supported by CO_2 sorption experiments in the SRD reactor (see SI Fig. S8) showing that CO_2 at these temperatures does not dissociate to Ni-CO. In the same SV range, at 350 °C Ni-CO coverage stays rather constant. At 400 °C at higher SV and at 350 °C in general, Ni-CO coverage is rather SV-independent, suggesting that carbonyls readily react to methane (path V ff. in Fig. 15) and are replenished via formate (path IV in Fig. 15) which therefore can be seen as the rate-determining step for this type of catalyst.

The good match between the data obtained from SV variation and spatially resolved analysis along the reaction coordinate clearly demonstrate that by applying the spatially resolved *operando* analytics with the SRD reactor presented, the location can be seen as a reciprocal measure of SV (feed flow rate per catalyst mass, which is a function of the reactor coordinate, see also Supporting Information, Fig. S9) and, thus, SV variation can be investigated without actually altering the feed flow rate, i.e., flow properties. In another recent work, the capabilities of the SRD reactor and of the evaluation approach presented were applied to study fluctuating feed conditions in even more detail (see [32]).

CRediT authorship contribution statement

Timo Engl: Writing – original draft, Visualization, Methodology, Investigation, Formal analysis. **David Kellermann:** Writing – original draft, Visualization, Methodology, Investigation, Formal analysis. **Jan Kopyscinski:** Writing – review & editing, Validation, Resources. **Hannsjörg Freund:** Writing – review & editing, Supervision, Resources, Funding acquisition, Conceptualization. **Michael Rubin:** Writing – review & editing, Visualization, Supervision, Funding acquisition, Conceptualization. **Roland Dittmeyer:** Writing – review & editing, Supervision, Resources.

Declaration of competing interest

The authors declare that they have no known competing financial interests or personal relationships that could have appeared to influence the work reported in this paper.

Acknowledgements

The authors acknowledge funding by the German Research Foundation (DFG) within the priority program SPP2080 “DynaKat” (KL 3223/1-1/-2 and FR 2918/3-1/-2). The authors also would like to thank Pakpong Roongruangsree and Steven Walker from the Catalytic & Plasma Engineering Laboratory at McGill University for their support in operating the catalytic plate reactor.

Appendix A and B. Supplementary data

Supplementary data and information to this article concerning the normalization procedure of the DRIFTS analysis, additional experimental data, additional information on the CFD modeling incl. study on mesh independency and data on the kinetic modeling can be found online at https://doi.org/10.1016/j.fuel.2026.140764.

Data availability

Relevant data discussed in this study can be found in machine readable form in Appendix B. Data beyond what is published within the main article and appendices will be made available upon request.

References

[1] United Nations, Paris Agreement 2015.
[2] Raya-Tapia AY, López-Flores FJ, Sánchez A, Martín M, Ramírez-Márquez C, Ponce-Ortega JM. Ind Eng Chem Res 2025;64(43):20379–403. https://doi.org/10.1021/acs.iecr.5c02274.
[3] Wang W, Nguyen-Quang M, Mateo D, Yong X, Li T, Xie H, et al. ACS Catal 2025;15(12):10868–96. https://doi.org/10.1021/acscatal.5c01422.
[4] Machhammer O, Janisch I. Chem Ing Tech 2024;96(8):1024–35. https://doi.org/10.1002/cite.202300197.
[5] Schmider D, Maier L, Deutschmann O. Ind Eng Chem Res 2021;60(16):5792–805. https://doi.org/10.1021/acs.iecr.1c00389.
[6] Kalz KF, Kraehnert R, Dvoyashkin M, Dittmeyer R, Gläser R, Krewer U, et al. ChemCatChem 2017;9(1):17–29. https://doi.org/10.1002/cctc.201600996.
[7] Bosco M, Vogel F. Catal Today 2006;116(3):348–53. https://doi.org/10.1016/j.cattod.2006.05.064.
[8] Choi J-S, Partridge WP, Pihl JA, Kim M-Y, Kočí P, Daw CS. Catal Today 2012;184(1):20–6. https://doi.org/10.1016/j.cattod.2011.11.007.
[9] Choi J-S, Partridge WP, Daw CS. Appl Catal A 2005;293:24–40. https://doi.org/10.1016/j.apcata.2005.06.025.
[10] Eck M, Lott P, Schweigert D, Börnhorst M, Deutschmann O. Chem Ing Tech 2022;94(5):738–46. https://doi.org/10.1002/cite.202100192.
[11] Hernandez Lalinde JA, Kofler K, Huang X, Kopyscinski J. Catalysts 2018;8(2):86. https://doi.org/10.3390/catal8020086.
[12] Horn R, Degenstein NJ, Williams KA, Schmidt LD. Catal Lett 2006;110(3–4):169–78. https://doi.org/10.1007/s10562-006-0117-8.
[13] Horn R, Williams KA, Degenstein NJ, Schmidt LD. Chem Eng Sci 2007;62(5):1298–307. https://doi.org/10.1016/j.ces.2006.11.030.
[14] Horn R, Williams KA, Degenstein NJ, Bitsch-Larsen A, Dalle Nogare D, Tupy SA, et al. J Catal 2007;249(2):380–93. https://doi.org/10.1016/j.jcat.2007.05.011.
[15] Kopyscinski J, Schildhauer TJ, Vogel F, Biollaz SMA, Wokaun A. J Catal 2010;271(2):262–79. https://doi.org/10.1016/j.jcat.2010.02.008.
[16] Sá J, Fernandes DLA, Aiouache F, Goguet A, Hardacre C, Lundie D, et al. Analyst 2010;135(9):2260. https://doi.org/10.1039/c0an00303d.
[17] Shakir O, Yezerets A, Currier NW, Epling WS. Appl Catal A 2009;365(2):301–8. https://doi.org/10.1016/j.apcata.2009.06.033.
[18] Urakawa A, Maeda N, Baiker A. Angew Chem 2008;120(48):9396–9. https://doi.org/10.1002/ange.200804077.
[19] Maeda N, Urakawa A, Baiker A. Top Catal 2009;52(13–20):1746–51. https://doi.org/10.1007/s11244-009-9342-x.
[20] Hyakutake T, Van Beek W, Urakawa A. J Mater Chem A 2016;4(18):6878–85. https://doi.org/10.1039/C5TA09461E.
[21] Van Beek L, Jain D, Gholkar P, Eldridge TJ, Nguyen HP, Muramoto K, et al. Catal Today 2024;429:114466. https://doi.org/10.1016/j.cattod.2023.114466.
[22] Engl T, Langer M, Freund H, Rubin M, Dittmeyer R. Chem Ing Tech 2023;95(5):658–67. https://doi.org/10.1002/cite.202200204.
[23] Weber S, Abel KL, Zimmermann RT, Huang X, Bremer J, Rihko-Struckmann LK, et al. Catalysts 2020;10(12):1471. https://doi.org/10.3390/catal10121471.
[24] Weber S, Zimmermann RT, Bremer J, Abel KL, Poppitz D, Prinz N, et al. ChemCatChem 2022;14(8):e202101878. https://doi.org/10.1002/cctc.202101878.
[25] Xu H-Y, Li Z-J, Cen J, Yao N. React Chem Eng 2025;10(12):2789–99. https://doi.org/10.1039/D5RE00231A.

[26] Strucks P, Failing L, Kaluza S. Chem Ing Tech 2021;93(10):1526–36. https://doi.org/10.1002/cite.202100049.
[27] Liu K, Nawaz MA, Liao G. Carbon Neutralization 2025;4(1):e190.
[28] Lalinde JAH, Jiang J, Jai G, Kopyscinski J. Chem Eng J 2019;357:435–46. https://doi.org/10.1016/j.cej.2018.09.161.
[29] Hernandez Lalinde JA, Roongruangsree P, Ilsemann J, Bäumer M, Kopyscinski J. Chem Eng J 2020;390:124629. https://doi.org/10.1016/j.cej.2020.124629.
[30] Tommasi M, Degerli SN, Ramis G, Rossetti I. Chem Eng Res Des 2024;201:457–82. https://doi.org/10.1016/j.cherd.2023.11.060.
[31] Weber D, Engl T, Raabe M, Hutzler A, Rubin M, Dittmeyer R, et al. Appl Catal A 2025;708:120582. https://doi.org/10.1016/j.apcata.2025.120582.
[32] Kellermann D, Engl T, Lipinski L, Dittmeyer R, Rubin M, Freund H. ChemCatChem 2026;18(10):e01657. https://doi.org/10.1002/cctc.202501657.
[33] Anderson SD, Kreitz B, Turek T, Wehinger GD. Ind Eng Chem Res 2022;61(30):10790–803. https://doi.org/10.1021/acs.iecr.2c01459.
[34] Surendran V, Bracconi M, Hernandez Lalinde JA, Maestri M, Kopyscinski J. Chem Eng J 2022;446:136999. https://doi.org/10.1016/j.cej.2022.136999.
[35] Engelbrecht N, Chiuta S, Everson RC, Neomagus HWJP, Bessarabov DG. Chem Eng J 2017;313:847–57. https://doi.org/10.1016/j.cej.2016.10.131.
[36] In Computer Aided Chemical Engineering, Vol. 48, Elsevier 2020.
[37] Hu T, Qin L, Zhou L, Zheng X, Zhu L-T. Chem Eng Sci 2026;321:123030. https://doi.org/10.1016/j.ces.2025.123030.
[38] Weber D, Wadlinger KM, Heinlein MM, Franken T. ChemCatChem 2022;14(20):e202200563. https://doi.org/10.1002/cctc.202200563.
[39] Levenspiel O. The Chemical Reactor Omnibook 2013.
[40] Agnelli M, Swaan HM, Marquez-Alvarez C, Martin GA, Mirodatos C. J Catal 1998;175:117–28.
[41] Aldana PAU, Ocampo F, Kobl K, Louis B, Thibault-Starzyk F, Daturi M, et al. Catal Today 2013;215:201–7. https://doi.org/10.1016/j.cattod.2013.02.019.
[42] Gamarra D, Munuera G, Hungría AB, Fernández-García M, Conesa JC, Midgley PA, et al. J Phys Chem C 2007;111(29):11026–38. https://doi.org/10.1021/jp072243k.
[43] Gamarra D, Martínez-Arias A. J Catal 2009;263(1):189–95. https://doi.org/10.1016/j.jcat.2009.02.012.
[44] Karelovic A, Ruiz P. J Catal 2013;301:141–53. https://doi.org/10.1016/j.jcat.2013.02.009.
[45] Li H, Jiao X, Li L, Zhao N, Xiao F, Wei W, et al. Catal Sci Technol 2015;5(2):989–1005. https://doi.org/10.1039/C4CY01237B.
[46] Raphulu MC, McPherson J. Gold Bull 2010;43:1.
[47] Solis BH, Cui Y, Weng X, Seifert J, Schauermann S, Sauer J, et al. PCCP 2017;19(6):4231–42. https://doi.org/10.1039/C6CP08504K.
[48] Franken T, Terreni J, Borgschulte A, Heel A. J Catal 2020;382:385–94. https://doi.org/10.1016/j.jcat.2019.12.045.
[49] Cárdenas-Arenas A, Quindimil A, Davó-Quiñonero A, Bailón-García E, Lozano-Castelló D, De-La-Torre U, et al. Appl Catal B 2020;265:118538. https://doi.org/10.1016/j.apcatb.2019.118538.
[50] Sichert S, Stahl S-F, Korup O, Horn R. ACS Catal 2024;14(11):8676–93. https://doi.org/10.1021/acscatal.4c00536.
[51] Kumar R, Sahoo APSK, Prabhakar JK, Ray K. Eur J Inorg Chem 2026;29(8):e202500543. https://doi.org/10.1002/ejic.202500543.
[52] Koschany F, Schlereth D, Hinrichsen O. Appl Catal B 2016;181:504–16. https://doi.org/10.1016/j.apcatb.2015.07.026.